Article

Direct Measurement of Radical-Catalyzed C_6H_6 Formation from Acetylene and Validation of Theoretical Rate Coefficients for C_2H_3 + C_2H_2 and C_4H_5 + C_2H_2 Reactions

Mica C. Smith, Guozhu Liu, Zachary J. Buras, Te-Chun Chu, Jeehyun Yang, and William H. Green*

Read Online

ACCESS | Metrics & More | Article Recommendations | SI Supporting Information

ABSTRACT: The addition of vinylic radicals to acetylene is an important step contributing to the formation of polycyclic aromatic hydrocarbons in combustion. The overall reaction $3C_2H_2 \rightarrow C_6H_6$ could result in large benzene yields, but without accurate rate parameters validated by experiment, the extent of aromatic ring formation from this pathway is uncertain. The addition of vinyl radicals to acetylene was investigated using time-resolved photo-ionization time-of-flight mass spectrometry at 500 and 700 K and 5−50 Torr. The formation of C_6H_6 was observed at all conditions, attributed to sequential addition to acetylene followed by cyclization. Vinylacetylene (C_4H_4) was observed with increasing yield from 500 to 700 K, attributed to the β-scission of the thermalized 1,3-butadien-1-yl radical and the chemically activated reaction $C_2H_3 + C_2H_2 \rightarrow C_4H_4 + H$. The measured kinetics and product distributions are consistent with a kinetic model constructed using pressure- and temperature-dependent reaction rate coefficients computed from previously reported *ab initio* calculations. The experiments provide direct measurements of the hypothesized C_4H_5 intermediates and validate predictions of pressure-dependent addition reactions of vinylic radicals to C_2H_2, which are thought to play a key role in soot formation.
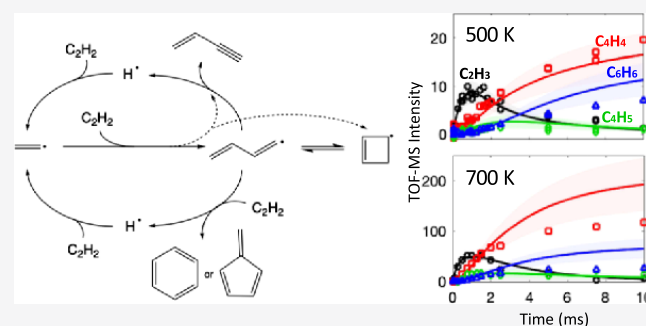
1. INTRODUCTION

Polycyclic aromatic hydrocarbons (PAHs) formed during incomplete combustion are an important class of atmospheric pollutants and serve as precursors for soot.[1−3] Understanding PAH chemistry, specifically the detailed chemical mechanisms and key radical reactions, is one of the most critical challenges for the development of efficient combustion engines with minimal environmental impact. It is thought that many PAHs are formed by hydrogen-abstraction-carbon-addition (HACA) mechanisms,[4−7] wherein acetylene (C_2H_2) addition reactions play a key role. The present study focuses on simple analogues to the HACA reaction sequence, in which benzene, the simplest aromatic ring, is formed by acetylene addition to two different vinylic radicals, C_2H_3 and n-C_4H_5.

Observations of the chemical composition of sooting flames suggest that reactions involving unsaturated radicals dominate the formation of aromatics under combustion conditions.[8−13] The reactions of several radicals (e.g., propargyl,[14−18] cyclopentadienyl,[19,20] and butadienyl[21−25]) implicated in benzene formation have been investigated. While the recombination of propargyl radicals has been identified as a primary route to benzene, it remains a matter of debate to what extent other radical reactions contribute to overall benzene yields.[3,12,26−30]

The addition of vinyl radical (C_2H_3) to C_2H_2 is a particularly interesting system because (1) it produces the butadienyl

radicals n-C_4H_5 and i-C_4H_5, both of which can react with C_2H_2 to form benzene; and (2) it can produce high yields of vinylacetylene (C_4H_4) and H atoms, which can reform C_2H_3 via H addition to the C_2H_2 reactant, such that the reaction products are continuously generated as long as C_2H_2 is present. The reactions of C_4H_5 radicals with C_2H_2 are thought to play a role in the formation of aromatic compounds in flames;[9,31,32] furthermore, vinylacetylene is expected to be an important source of radicals in acetylene pyrolysis at some conditions, as well as formation of larger PAHs.[33−36] The high concentrations of C_2H_2 observed in sooting flames[37,38] suggest that, in addition to the propargyl radical self-reaction, C_2H_3 addition to C_2H_2 may be a key step in the formation of aromatics, PAHs, and soot. These reactions also play a role in the exothermic polymerization of acetylene, which can create safety hazards in the use of compressed acetylene for various applications.
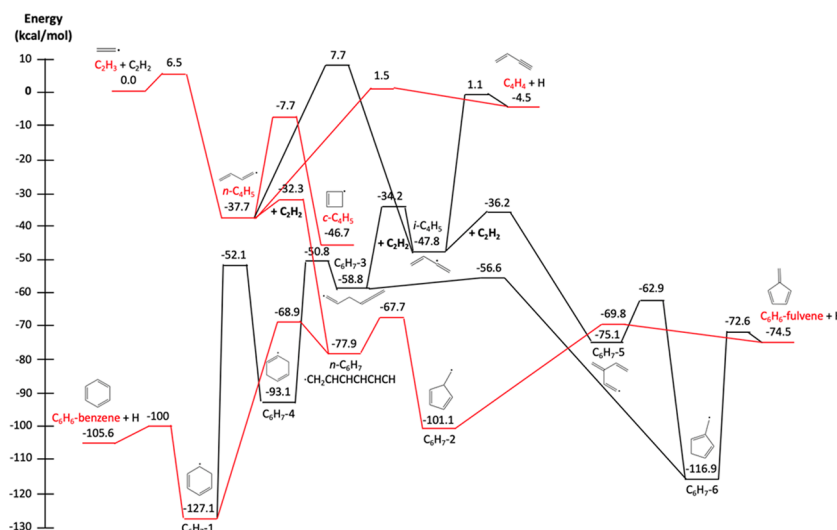
To assess the relative importance of benzene formation channels, accurate reaction rate constants and product
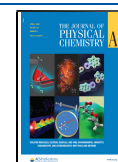
Figure 1. Potential energy surface showing calculated relative energies for the $C_2H_3 + C_2H_2$ and $C_4H_5 + C_2H_2$ reactions leading to C_6H_6 formation. The C_4H_5 surface was calculated by Ribeiro and Mebel using the CCSD(T)-F12//B2PLYPD3 method;[46] the C_6H_7 surface was calculated by Senosiain and Miller at the rQCISD(T) level of theory.[24] Red lines indicate pathways considered in the model derived in this work; red text indicates species validated in this work with photoionization time-of-flight mass spectrometry.

branching ratios are needed. The formation of products in the reaction of C_2H_3 with C_2H_2 has been investigated at various conditions in a few experimental works. Callear and Smith generated C_2H_3 radicals by photolyzing H_2 in the presence of various concentrations of C_2H_2 and measured the yields of C_2H_4, C_4H_6, C_6H_6 (benzene), and C_6H_8 (*trans*-1,3,5-hexatriene) using gas chromatography.[21] By assuming the steady-state approximation for radical intermediates and fitting to a complex mechanism, they indirectly estimated the reaction rate constant k_1 of R1 relative to the reaction of C_2H_3 with H_2 at 300 and 400 K and a pressure of 500 Torr, conditions for which R1 is likely in the high-pressure limit. Using their reported ratios along with temperature-dependent rate coefficients for $C_2H_3 + H_2$ from a combined experimental and theoretical analysis[39] gives values of $\sim 2 \times 10^{-16}$ cm^3 s^{-1} for k_1 at 300 K and $\sim 3 \times 10^{-15}$ cm^3 s^{-1} at 400 K.

$$C_2H_3 + C_2H_2 \rightleftharpoons n\text{-}C_4H_5 \qquad (R1)$$
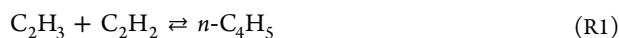
Fahr and Stein[40] measured the rate constant of R2 in a Knudsen-cell pyrolysis flow reactor using mass spectrometry at 1023−1273 K and 1−10 mTorr and suggested a rate constant expression relative to the overall rate of the self-reaction of C_2H_3. Using a directly measured rate coefficient for the C_2H_3 self-reaction[41] with the reported ratio at 1273 K yields an estimated value of $\sim 3 \times 10^{-13}$ cm^3 s^{-1} for k_2; note that the measurements of ref 41 were conducted at a higher pressure and lower temperature range than Fahr and Stein's measurements, which may affect the accuracy of this value of k_2.

$$C_2H_3 + C_2H_2 \rightleftharpoons C_4H_4 + H \qquad (R2)$$

Kubitza generated C_2H_3 using Na and vinyl iodide and measured the reaction rate of R2 at 623 K and 2 Torr, quantifying C_2H_3 and C_4H_4 concentrations using mass spectrometry and obtaining a value for k_2 of $\sim 1 \times 10^{-13}$ cm^3 s^{-1}.[42] Knyazev et al. investigated the reaction kinetics of $C_2H_3 + C_2H_2$ using laser flash photolysis with time-resolved photo-ionization mass spectrometry at 630−980 K and 4−12 Torr, measuring the appearance of C_4H_4 only and assuming that the reaction proceeds solely via channel R2 under their conditions.[43] Their reported Arrhenius expression yields k_2 values ranging

from 2.65×10^{-14} cm^3 s^{-1} at 630 K to 1.47×10^{-13} cm^3 s^{-1} at 980 K.

In addition to these experimental works, several theoretical studies have explored the $C_2H_3 + C_2H_2$ system. Weissman and Benson used a combination of the transition-state theory and the experimental measurements of Callear and Smith[21] at 300 K to estimate pre-exponential factors and activation energies, which were then used to predict the temperature dependence of k_1 at the high-pressure limit.[44] They reported rate coefficients of 6.19 $\times 10^{-16}$ and 2.59×10^{-15} cm^3 s^{-1} at 300 and 400 K, respectively. Wang and Frenklach used the Rice−Ramsperger−Kassel−Marcus (RRKM) theory to compute pressure-dependent rate constants for both R1 and R2 with a pseudo-strong-collider assumption, using molecular parameters corrected to reproduce experimental data.[22] Later, Miller et al. used the electronic structure theory (DFT-B3LYP and a G2-like method) to calculate properties of stationary points on the C_4H_5 potential energy surface, an RRKM analysis to compute microcanonical rate constants, and solutions to the time-dependent, multiple-well master equation to extract information on the total rate constant and product distributions as a function of temperature and pressure.[45] Their calculated rate coefficients agreed with previous experimental measurements[21,40,43] within a factor of 2. They predicted that R1, R2, and the formation of the 4-membered ring cyclic isomer $c\text{-}C_4H_5$ (R3) all contribute to consumption of C_2H_3 at temperatures up to 800 K. Recent work by Ribeiro and Mebel treated the C_4H_5 surface at a higher level of theory, examining a comprehensive set of reactions including $C_2H_3 + C_2H_2$ using the CCSD(T)-F12//B2PLYPD3 method.[46] The energies calculated by Ribeiro and Mebel[46] for the $C_2H_3 + C_2H_2$ potential energy surface are shown in Figure 1.

$$C_2H_3 + C_2H_2 \rightleftharpoons c\text{-}C_4H_5 \qquad (R3)$$

The previous work indicates that under typical combustion conditions, R2 is the dominant channel for $C_2H_3 + C_2H_2$ and is relatively insensitive to pressure at those conditions. However, from 300 to 700 K, the conditions of most laboratory measurements, R1 and R3 also become important and all three rate coefficients are expected to be significant functions of

pressure. (The channel leading to formation of i-C_4H_5, while possibly important under high-temperature and low-pressure conditions, is not expected to play a role in lower-temperature conditions due to the high barrier to isomerization from n-C_4H_5; see Figure 1.) Hence, measurements at one set of pressure and temperature conditions may not be applicable to other conditions, which might explain the discrepancy in reaction rates measured near 630 K at different pressures.[42,43] A thorough understanding of the C_4H_5 potential energy surface, through validation of the theoretical calculations with direct experimental measurements at a variety of temperatures and pressures, is therefore needed to accurately describe the chemistry of $C_2H_3 + C_2H_2$.

The addition of n-C_4H_5 to C_2H_2 to form an aromatic ring has only been explored in a few studies, theoretically and through indirect measurements, despite its presumed importance in a variety of chemical mechanisms devised to model sooting flames.[12,23,27,29] Callear and Smith reported rate constant ratios for R4 relative to $C_4H_5 + H_2$ of 10.4 (9.2) at 300 (400) K; using rate parameters reported by Weissman and Benson[44] for $C_4H_5 + H_2$ yields k_4 values of 2.4×10^{-15} cm^3 s^{-1} (1.2×10^{-14} cm^3 s^{-1}).[21] Wang and Frenklach performed semiempirical quantum mechanical calculations of several channels for the reaction of n-C_4H_5 with C_2H_2, including C_6H_7, acyclic C_6H_6, and benzene formation pathways, using molecular parameters corrected to match experimental data.[22] Westmoreland et al. combined measurements of benzene production in C_2H_2/O_2 flames with bimolecular quantum-RRK calculations of the pressure-dependent rate constants, which also used input parameters taken from previous measurements.[23] Their Arrhenius expression for R4 yields 4.2×10^{-15} cm^3 s^{-1} for k_4 at 400 K and 1 atm, slightly lower than the value reported by Callear and Smith.

$$C_4H_5 + C_2H_2 \rightleftarrows C_6H_6 + H \tag{R4}$$

More recently, Senosiain and Miller performed rQCISD(T) calculations and used the RRKM theory to predict pressure-dependent rate coefficients for n-C_4H_5 addition to C_2H_2; their calculations are summarized in Figure 1.[24] In contrast to earlier studies, their calculations indicated that aromatic ring formation in R4 proceeds via two distinct channels producing benzene and fulvene. At 300 (400) K and 1 atm, their Arrhenius expression predicts a roughly 2:1 ratio of benzene to fulvene with a combined rate constant k_4 of 3.6×10^{-17} cm^3 s^{-1} (1.2×10^{-15} cm^3 s^{-1}). Their calculations indicate that stabilized C_6H_7 may also be formed under some conditions. There are several different acyclic isomers and conformers of C_6H_7, which would be expected to react and interconvert at different rates. Senosiain and Miller considered a species $CH_2CHCHCHCHCH$ (referred to as n-C_6H_7 in Figure 1), which may exist in cis or trans conformers with varying reactivities. Other C_6H_7 isomers may also play a role in the n-$C_4H_5 + C_2H_2$ reaction; e.g., investigations of the hydrogen-assisted isomerization of fulvene to benzene identify a two-step isomerization pathway connecting C_6H_7-2 to C_6H_7-6.[47−49] A detailed consideration of the C_6H_7 potential energy surface, while outside the scope of this work, would be worthwhile to more accurately describe the pressure dependence of benzene and fulvene formation in this system.

The value of k_4 calculated by Senosiain and Miller is insensitive to pressure below 1 atm, similar to the results of Westmoreland et al. The k_4 values derived from the experiments of Callear and Smith[21] are at least a factor of 2 larger than the theoretical predictions of Senosiain and Miller, although it

should be noted that the temperatures of these experiments (300 and 400 K) fall outside the range of Senosiain and Miller's Arrhenius fit. A possible explanation for the difference is that Callear and Smith did not consider the C_2H_3 self-reaction in their reaction mechanism; instead, they assumed that all of the C_4H_6 they measured was formed by the reaction of C_4H_5 with H_2. Since the self-reaction can also form C_4H_6, this omission would affect their interpretation of the measured $[C_4H_6]/[C_6H_6]$ and lead to an artificially large k_4. Furthermore, since these values are derived from rate ratios relative to the rate constant of n-$C_4H_5 + H_2$, uncertainty in the latter value (which in this work was taken from Weissman and Benson[44] who also based their calculations on indirect experimental measurements) could contribute to the discrepancy. For these reasons, we recommend against the use of the k_4 value provided by Callear and Smith.[21]

The temperature-dependent rate coefficients for R1, R2, and R4 reported in previous experimental and theoretical works are summarized in Figure 2. The scarcity of direct measurements for the above reactions, variations up to an order of magnitude or more in calculated values of k_1 and k_4, and the lack of experimental validation of the pressure-dependent rate constants for R1 and R4 at temperatures above 400 K indicate that further investigation is needed to properly characterize these reactions. Moreover, the regeneration of C_2H_3 due to H addition to C_2H_2, though significantly reversible at typical combustion temperatures, is sensitive to pressure and may affect the formation of products under laboratory conditions. Due to the relative complexity of the $C_2H_3 + C_2H_2$ system, relying on a combination of uncertain rate estimates for elementary steps within a larger mechanism will lead to large uncertainties in predicted benzene and PAH yields.

In this work, reaction kinetics and product branching for $C_2H_3 + C_2H_2$ were directly measured at temperatures of 500 and 700 K and pressures ranging from 5 to 50 Torr using time-resolved photoionization time-of-flight mass spectrometry. We report time-resolved concentration profiles of C_2H_3, C_4H_4, C_4H_5, C_6H_6, and other key reaction products, as well as the sensitivity of product yields and branching ratios to temperature and pressure. The experimental time profiles are compared with the predictions of a kinetic model constructed using previous theoretical and experimental rate parameters[24,41,46,50] to assess the validity of these calculated values for describing PAH formation. The results provide detailed validation of theoretical rate coefficients, which can be used to extrapolate to combustion-relevant conditions in kinetic mechanisms to better understand the production of soot in a wide range of combustion processes.

2. METHODS

2.1. Photoionization Mass Spectrometry Measurements. All of the kinetics experiments were carried out using time-resolved photoionization time-of-flight mass spectrometry (PI-TOF-MS) in the Combustion Dynamics Laboratory at Massachusetts Institute of Technology.[51,52] The apparatus has been characterized in detail in ref 51 and is only briefly described here; a schematic diagram of the apparatus is provided in the Supporting Information. The apparatus consists of an 86 cm long cylindrical quartz reaction cell with a "bowtie" geometry (i.d. 1.6 cm in the central sampling region) wrapped with nichrome wire and enclosed in a stainless steel high-vacuum chamber ($P \sim 10^{-5}-10^{-8}$ Torr). The cell temperature was controlled using four K-type thermocouples to produce a
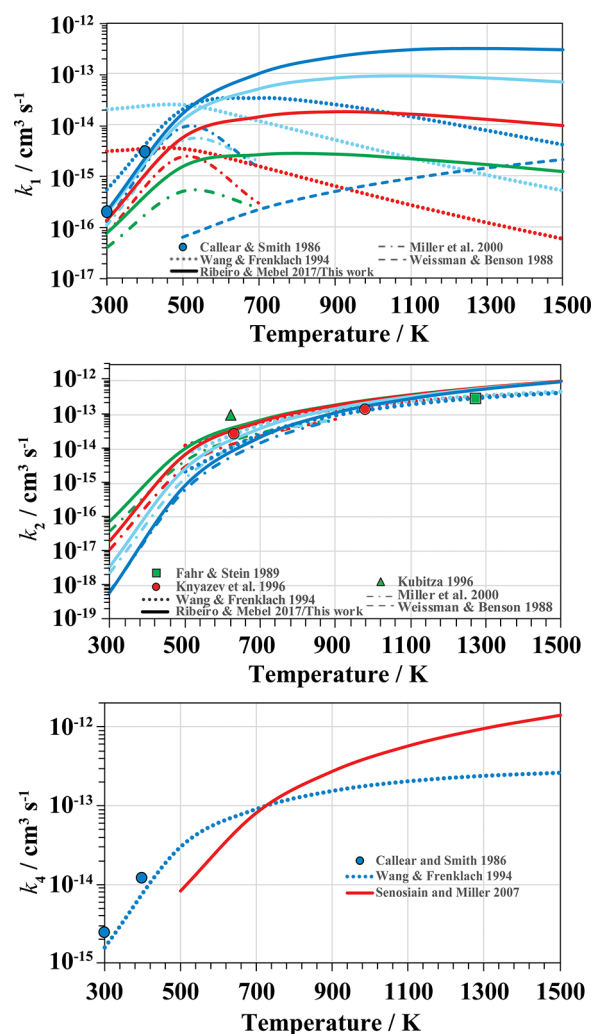
Figure 2. Comparison of experimental and theoretical rate coefficients reported in various works[21,22,40,42−45] for $C_2H_3 + C_2H_2 \rightleftarrows n\text{-}C_4H_5$ (R1, top), $C_2H_3 + C_2H_2 \rightleftarrows C_4H_4 + H$ (R2, middle), and $n\text{-}C_4H_5 + C_2H_2 \rightleftarrows C_6H_6 + H$ (R4, bottom). Rate constants from this work (solid lines) were determined using the quantum chemistry calculations of Ribeiro and Mebel.[46] Green lines correspond to low pressure (2 Torr and lower); red, 10 Torr; light blue, 100 Torr; and dark blue, 760 Torr. Symbols represent experimental measurements with colors corresponding to the pressure regime: blue circles are measurements by Callear and Smith[21] conducted at 500 Torr; red circles are measurements by Knyazev et al.[43] at 4−12 Torr; green squares are measurements by Fahr and Stein[40] at 1−10 mTorr; and green triangle is a measurement by Kubitza[42] at 2 Torr. The present measurements validate the red solid curve from 500 to 800 K.

uniform temperature profile (standard deviation ±2%) throughout the overlap region of the photolysis and absorption lasers. C_2H_2 (Airgas) was purified online with an activated charcoal trap (Airgas) to remove the acetone stabilizer. The purity of C_2H_2 after the trap was >99.9%, confirmed by GC-FID (GC 2014, Shimadzu). The flow rates of C_2H_2 and helium bath gas were regulated by calibrated mass flow meters (MKS Instruments). The pressure inside the reactor was monitored by a capacitance manometer and adjusted by increasing or decreasing the flow rate of helium and throttling a butterfly valve downstream of the reactor to achieve the desired pressure while holding constant the concentrations of C_2H_2 and vinyl iodide precursor as well as the residence time inside the reactor.

C_2H_3 radicals were produced from the photodissociation of vinyl iodide (Oakwood Chemical, 95% purity, degassed by several freeze−pump−thaw cycles) using 266 nm light from the fourth harmonic of a pulsed Nd:YAG laser (Spectra Physics Quanta Ray) operating at about one flash per second. The photolysis beam diameter (around 1.6 cm) was measured before each run, and the photolysis intensity (below 45 mJ cm^{-2} per pulse) was carefully selected to avoid possible multiphoton photodissociation of either C_2H_2 or any leftover acetone impurity.[43] Experiments with C_2H_2 in the absence of vinyl iodide were performed to confirm that C_2H_2 photolysis is negligible under our conditions (see the Supporting Information). The repetition rate of the photolysis laser and the total gas flow rate were maintained such that the contents of the reaction cell were completely refreshed between photolysis flashes. The concentration of vinyl iodide was usually kept at $\sim 5 \times 10^{14}$ molecules cm^{-3}, which gave an initial concentration range of C_2H_3 radical on the order of 10^{11}−10^{12} molecules cm^{-3} with changing photolysis intensity, pressure, and temperature. Such low concentrations were necessary to minimize the possible influence of the C_2H_3 radical self-reaction.

The central section (with a length of 30 cm and i.d. 1.6 cm) of the reaction cell is designed to enable time-resolved direct measurement of products with PI-TOF-MS.[51] A sampling pinhole (0.2 mm) is centrally located in the upper wall of the reactor. Gas sampled through the pinhole passes through a skimmer in free jet flow to form a molecular beam. In this manner, the reactive species are effectively "frozen" before entering the ionization region, such that the rapid cooling in the molecular beam prevents further reactions from taking place. Molecules in the beam were photoionized using 118.2 nm (10.487 eV) light generated by focusing the third harmonic (355 nm) output of a pulsed Nd:YAG laser (Quantel Brilliant, <12 ns full width at half maximum (FWHM) pulses, repetition rate set to match the photolysis laser) in a $\sim$1:10 Xe/Ar gas cell. The relative ion abundance was analyzed using a reflectron TOF-MS and detected using a discrete dynode electron multiplier detector and analog preamplifier (Kore). The time-of-flight spectra were converted to mass-to-charge ratios (m/z) by calibration with a mixture of stable species at known concentrations (Airgas, 100 ppm each propene, 1,3-butadiene, benzene, furan, cyclohexane, toluene, and n-heptane in helium).

Relative time-dependent signals of the reactants and products following photolysis were monitored by scanning the delay time of the photoionization laser pulse relative to the photolysis laser. The time delays ranged from a few hundred microseconds, set by the time lag as species flow through the sampling pinhole, to 10 ms, after which side and wall reactions start to complicate the observed time profiles. At each reaction time point, mass spectra were averaged over 150 photolysis flashes. Background mass spectra were also collected at a negative delay time by firing the photoionization laser before the photolysis laser pulse.

To compare the measured TOF-MS signals to absolute species concentrations, the peak at a given m/z at each delay time was integrated to give the average signal intensity. The background signal intensity was subtracted from all signal intensities for each m/z of interest. In the case of signals corresponding to n-C_4H_5 (m/z 53) and C_6H_7 (m/z 79), there is a significant contribution to the signal intensity from the natural abundance of ^{13}C (1.1%) in C_4H_4 (m/z 52) and C_6H_6 (m/z 78). To account for this contribution, the ^{13}C abundance of C_4H_4 (4.4% of the signal intensity at m/z 52) was subtracted from all signal intensities at m/z 53, and the ^{13}C abundance of C_6H_6

(6.6% of the signal intensity at m/z 78) was subtracted from all signal intensities at m/z 79. A similar procedure was performed to correct the signals at other m/z values of interest that may also have contributions from ^{13}C (e.g., m/z 54 or 80); however, since the signals at m/z 53 and 79 are always very small due to the low photoionization cross sections (PICS) of radicals (see the next paragraph), the signal arising from their ^{13}C analogues is negligible.

For each of the TOF-MS experiments, several time points were taken in which a small amount (typically 5 sccm) of the calibration gas mixture was flowed together with the reactants and buffer gas. The calibration gas signals were independent of the reaction time, and experiments were performed with and without the calibration mixture to confirm that they do not influence the $C_2H_3 + C_2H_2$ reaction system. The integrated signal intensities of each calibration species were averaged at the corresponding m/z over all delay times and used to calculate a calibration factor $R_i = \frac{A_i}{\sigma_i C_i}$ where the index i corresponds to the calibration species, A is the average integrated signal intensity of that calibration species, C is the known concentration of the calibration species, and σ is the photoionization cross section (PICS) of the calibration species (see the Supporting Information for PICS values used in this work). While in some cases R_i has been found to have a linear dependence on the m/z value,[52] in the present work no clear dependence was observed, so the R_i values at each m/z were averaged to obtain the average calibration factor R.

2.2. Kinetic Model. A pressure-dependent kinetic model was constructed to compare the experimental TOF-MS time profiles with theoretical predictions, including the reaction of C_2H_3 with C_2H_2 (R1−R3), reactions of n-C_4H_5 (R4 and the isomerization of n-C_4H_5 to c-C_4H_5), the reaction of H with C_2H_2 to regenerate C_2H_3 (R5), and the self-reaction of C_2H_3 (R6). The full mechanism is given in the Supporting Information. Rate constants for R1−R3 were determined using the master equation solver package Arkane,[53] which uses the transition-state theory to compute pressure-dependent rate parameters from previously reported theoretical calculations.[46,50] Rate constants for the various channels of n-$C_4H_5 + C_2H_2$ were taken from the predictions by Senosiain and Miller: the formation of benzene, fulvene, and C_6H_7 (the rate for which was reported as the sum of C_6H_7 isomers and is assumed in this work to primarily form the cyclohexadienyl radical, or C_6H_7-1 in Figure 1).[24] The calculations were performed assuming the modified strong collision approximation, and Lennard-Jones parameters for collisions between He and C_4H_5 radical species were determined using the values of ε and σ estimated by the Joback method implemented in the reaction mechanism generator (RMG).[54,55] The collisional energy transfer parameters assuming the exponential down model $<\Delta E_{down}> = \alpha_0 (T/T_0)^n$ were taken from Ribeiro and Mebel.[46] The RRKM theory was applied to compute phenomenological rate coefficients $k(T,P)$ fitted into the Chebyshev format; the resulting rate coefficients are given in the Chemkin-format file in the Supporting Information. Thermochemical parameters used to determine reverse rate coefficients were obtained using available open-source data in the NASA polynomial format available in RMG's thermochemistry database. Further details on the thermochemistry sources are found in the Supporting Information. More details on the simulation method used here can be found in a recent publication.[56]

For $C_2H_3 + C_2H_3$, there are three main channels for the reaction as shown in R6a−R6c. Although some of these channels can be observed in the experiment, they are not expected to affect the $C_2H_3 + C_2H_2$ reaction (see Section 3 for a more detailed discussion). Thus, the overall reaction R6 was used in the model to account for the self-reaction of C_2H_3, the kinetics of which were measured in laser absorption experiments by Ismail et al.,[41] and a 100% yield of C_4H_6 was assumed.

$$H + C_2H_2 \rightleftharpoons C_2H_3 \tag{R5}$$

$$C_2H_3 + C_2H_3 \rightleftharpoons C_4H_6 \tag{R6a}$$

$$C_2H_3 + C_2H_3 \rightleftharpoons C_2H_2 + C_2H_4 \tag{R6b}$$

$$C_2H_3 + C_2H_3 \rightleftharpoons CH_3 + C_3H_3 \tag{R6c}$$

$$C_2H_3 + C_2H_3 \rightleftharpoons \text{products} \tag{R6}$$
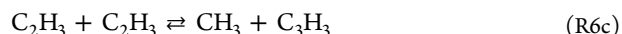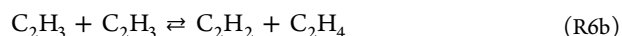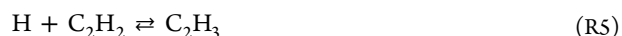
The resulting mechanism, containing the main reaction pathways of $C_2H_3 + C_2H_2$ and n-$C_4H_5 + C_2H_2$, is referred to as model 1, and full details are given in the Supporting Information. This mechanism was found to be sufficient to describe the chemistry inside the reactor at short reaction times, as seen in the following sections. However, at longer reaction times (>2 ms), several side reactions complicate the observed kinetic traces, particularly reactions involving I atom; evidence for this can be seen in the measured traces at m/z 127 and 128 (Supporting Information), which indicate gradual consumption of the I atom and formation of HI over a time scale of 10 ms. Therefore, an extended mechanism was constructed, containing model 1 as the base mechanism and adding a number of side reactions with rates taken from the literature or estimated. This mechanism, referred to as model 2, was used to assess the impact of various side processes on C_4H_4 and C_6H_6 formation at the longer time scales needed to observe secondary chemistry (i.e., the second C_2H_2 addition leading to aromatic ring formation, in contrast to the first C_2H_2 addition to C_2H_3, which is considered primary chemistry). See Section 3.3 for a detailed discussion of the reactions included in model 2.

Models 1 and 2 were simulated under our experimental conditions as a homogeneous batch reactor at constant temperature and pressure. Although C_2H_3 radicals are produced immediately after the photolysis pulse, there is a delay of several hundred microseconds associated with sampling from the irradiated volume to the pinhole and then to the MS detection region, which must be accounted for in the model. The sampling time constant was estimated by fitting the rise time of the signal at m/z 127 after photolysis, corresponding to the formation of the I atom, using the method of Buras et al.[52] Due to the convoluted effects of molecular beam sampling, chemical reaction of the reactive C_2H_3 radical, and the rapid regeneration of C_2H_3 from R5, the initial C_2H_3 concentration for the TOF-MS experiments cannot be reliably determined from the signal at m/z 27. The concentration of the C_2H_3 radical, $[C_2H_3]_0$, in the model was therefore determined by estimating the initial concentration of the I atom from the signal at m/z 127 (see the Supporting Information), which is assumed equal to $[C_2H_3]_0$.

The modeled species concentrations at each experimental condition were converted to predicted TOF-MS signals to compare with the measured signal intensities, using the expression $A_j = C_j R \sigma_j$, where the index j corresponds to the reactant or product species at a given m/z, A is the average integrated signal intensity of the species, C is the modeled
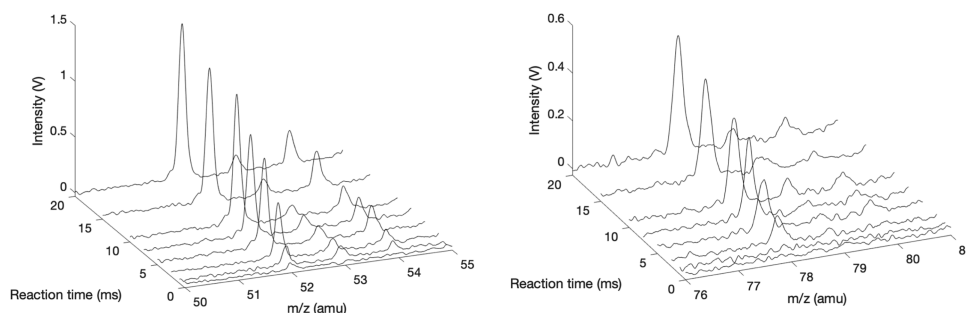
Figure 3. Background-corrected time-of-flight mass spectra showing the appearance of products at m/z 52, 53, 54, 78, 79, and 80 at various delay times for the experiment at 500 K and 25 Torr. $[C_2H_2]$: 3×10^{16} cm^{-3}.

concentration for the species, R is the experimentally derived calibration factor for each condition (see Section 2.1), and σ is the PICS of the species. Given the uncertainties in the PICS values, and the uncertainty in the calibration factors R for each experimental condition, which are affected by uncertainties in the reactor temperature and gas flow rates, the estimated uncertainty of the modeled signal intensities would be 25–50% if the model $C(t)$ were exact. These uncertainties due to σ and R are shown as shaded bands in the following figures. Note that there are often more than one species in the model with the same m/z contributing to the total predicted signal $A = \sum_j A_j$,

which increases the magnitude of the overall uncertainty.

3. RESULTS AND DISCUSSION

3.1. Products Observed by TOF-MS. Several species (both reactants and products) were detected and identified by PI-TOF-MS after the photolysis pulse. The I atom (m/z 127) appears in the mass spectrum rapidly after photolysis, along with the C_2H_3 radical at m/z 27. At longer reaction times, species at m/z 52 (C_4H_4), 53 (C_4H_5), 54 (C_4H_6), and 78 (C_6H_6) were identified as the major reaction products based on their clear time-dependent concentration profiles. Smaller time-dependent signals at m/z 15, 39, 79, 80, 128, and 180 were also observed and are discussed in the following paragraphs. Background peaks at m/z 54, 68, 78, 84, 92, and 100 correspond to the species in the calibration mixture; this time-independent background was removed by subtracting the mass spectral signal acquired at a delay time before the photolysis flash (typically −200 μs). Representative time-dependent mass spectra of the key reaction products are shown in Figure 3; mass spectra showing the rise and decay of C_2H_3 are shown in the Supporting Information.

As discussed above, the $C_2H_3 + C_2H_2$ reaction leads to production of C_4H_5, C_4H_4, and C_6H_6 products, as well as H atoms, which can recombine with C_2H_2 to regenerate the C_2H_3 radical. The resulting catalytic cycle is illustrated in Scheme 1. These products were all observed with TOF-MS as seen in Figure 3, and the steadily increasing signals of m/z 52 (C_4H_4) and m/z 78 (C_6H_6) over long reaction times up to 20 ms confirm the importance of the catalytic cycle, which continuously generates more products. As discussed below, the total yield of C_4 and C_6 products is significantly larger than the number of radicals formed by the photolysis flash.

For some species, a number of isomers are expected to contribute to the signal at the same m/z. For instance, several isomers are possible for the m/z 78 species produced in this system, including several different linear C_6H_6 isomers (l-C_6H_6), fulvene, and benzene. Under our experimental conditions, the

Scheme 1. Catalytic Cycle Producing C_4H_4 and C_6H_6 from C_2H_3 in the Presence of C_2H_2[a]
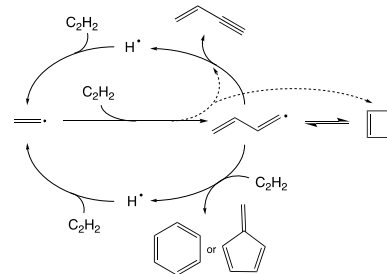
[a]Dashed lines indicate chemically activated reactions, which are important at high-temperature and low-pressure conditions. For clarity, the short-lived minor product C_6H_7 (nearly 100% of which proceeds to formation of C_6H_6 + H) is omitted from this scheme.

branching to benzene is predicted to dominate over fulvene and l-C_6H_6 according to the theoretical analyses of Wang and Frenklach[22] and Senosiain and Miller.[24] We note that the adduct C_6H_7 can also be formed, and indeed a small signal at m/z 79 can be observed in some conditions (see Figure 3 and Supporting Information), but in this work, we mainly focus on the formation of the major C_6H_6 product. Previous studies incorporating both experimental data and theoretical calculations have concluded that acyclic C_6H_6 formation is 2–3 orders of magnitude slower than benzene or fulvene formation under our conditions,[22−24] so this minor pathway was omitted from the simplified model used in this work. Fulvene is known to undergo H-assisted isomerization to benzene as noted above; we assessed the impact of this reaction pathway by including the high-pressure limit rate coefficients calculated by Jasper and Hansen[49] in our model and found that fulvene isomerization is negligible under our conditions. According to theoretical studies,[45,46] the important isomers for the m/z 53 species under our reaction conditions are n-C_4H_5 and the 4-membered ring c-C_4H_5, as illustrated in Scheme 1 and Figure 1 (the more stable i-C_4H_5 becomes significant only at temperatures above 800 K).

In addition to the major reactions R1−R4, some C_2H_3 is consumed by self-reaction even at the low initial radical concentrations used in these experiments. The appearance of butadiene at m/z 54, as well as small signals corresponding to the methyl radical at m/z 15 and the propargyl radical at m/z 39 (see Figures S5 and S6 in the Supporting Information), suggests the presence of the self-reaction channels R6a−R6c (C_2H_4 and C_2H_2 have ionization energies above 10.5 eV and thus cannot be observed in our experiment). The production of the propargyl radical via the C_2H_3 self-reaction or through reaction of the methyl radical with C_2H_2 might lead to the formation of
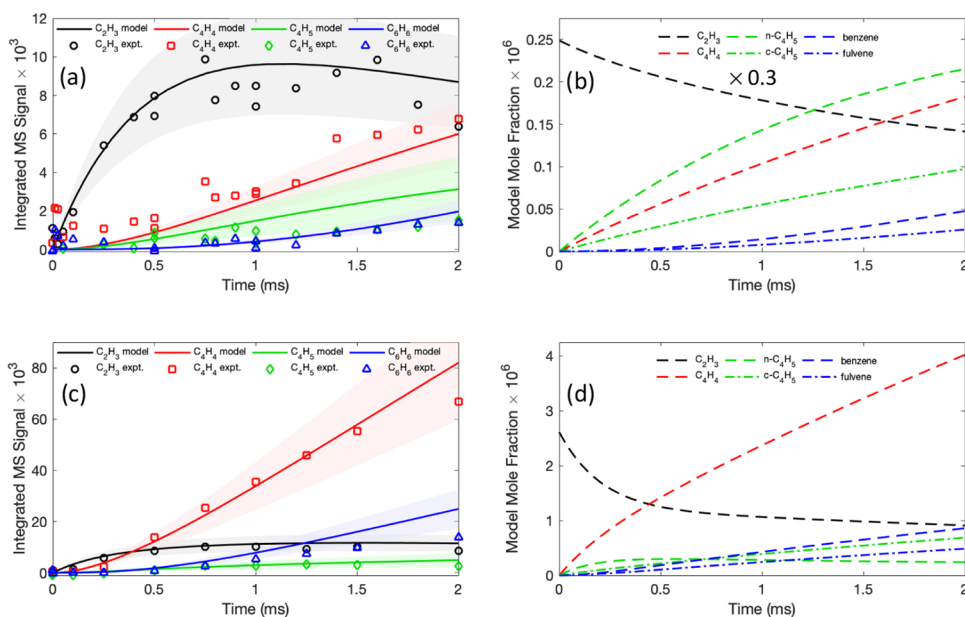
Figure 4. Temperature dependence of measured and modeled TOF-MS signal intensities and modeled species concentrations predicted by model 1 at various delay times after photolysis (time 0). Black circles correspond to the experimental signal for m/z 27 (C_2H_3); red squares, m/z 52 (C_4H_4); green diamonds, m/z 53 (C_4H_5); and blue triangles, m/z 78 (C_6H_6). Solid black, red, green, and blue lines correspond to the modeled signal intensities for C_2H_3, C_4H_4, C_4H_5, and C_6H_6, respectively. Dashed black lines indicate the modeled concentration of C_2H_3 (scaled by a factor of 0.3 for 500 K); dashed red lines, C_4H_4; dashed green lines, n-C_4H_5; dot-dash green lines, c-C_4H_5; dashed blue lines, benzene; and dot-dash blue lines, fulvene. Concentration of C_2H_2: 3×10^{16} cm^{-3}. (a, b) 500 K, 25 Torr, $[C_2H_3]_0$ in model = 4×10^{11} cm^{-3}; (c, d) 700 K, 25 Torr, $[C_2H_3]_0 = 9 \times 10^{11}$ cm^{-3}.

benzene; furthermore, the production of a H atom in these processes may influence the regeneration of the C_2H_3 radical via R5. To assess the impact of propargyl and methyl radicals on the reactions of interest, the vinyl self-reaction R6 in the model was adjusted to assume 100% yield of $CH_3 + C_3H_3$, and the reactions $CH_3 + C_2H_2 \rightarrow$ products (using the theoretical high-pressure limit rate coefficients by Diau et al.[57] and assuming the products are 100% C_3H_3 plus two H atoms) and $C_3H_3 + C_3H_3 \rightarrow$ products (using the experimental rate coefficient by Shafir et al.[18] and assuming 100% yield of benzene) were added. The effect on the modeled concentration of C_6H_6 and other products was found to be negligible at all of the conditions in this work. Thus, side reactions involving propargyl radical recombination are not expected to compete with the main reactions of radicals with acetylene at our reaction conditions.

3.2. Temperature and Pressure Dependence. The integrated signal intensities for reactants and products were compared with the model predictions as described in Section 2.2 to assess the validity of the rate parameters derived from recent theoretical calculations.[24,46] (Sensitivity analysis for the major reaction products is given in the Supporting Information.) Figure 4 shows the experimental and predicted time-resolved TOF-MS signal intensities and the modeled concentrations using model 1 in the $C_2H_3 + C_2H_2$ reaction at 25 Torr and temperatures of 500 and 700 K, for reaction times up to 2 ms. (A comparison of the experimental data with model 2, to evaluate the impact of side chemistry at longer reaction times, is given in Section 3.3.)

Photolysis of the vinyl iodide precursor produces a rapid observed rise in C_2H_3 within 1 ms followed by a decay and rise of the major products C_4H_4, C_4H_5, and C_6H_6. At 500 K, as seen in Figure 4b, the rate of R1 is slightly faster than R2, and a slow but significant rise in C_6H_6 is observed due to R4. At 700 K, as seen in Figure 4d, the $C_2H_3 + C_2H_2$ overall reaction rate increases and the rate of R2 becomes considerably faster relative to R1, as well-

skipping to the H-loss channel is favored at higher temperatures. The rate of R4 also increases, and somewhat more C_6H_6 is formed despite the shift in branching to favor C_4H_4 over n-C_4H_5. H atoms formed in R2 and R4 react with C_2H_2 to regenerate C_2H_3 radicals (R5), which even within the first 2 ms leads to product yields much greater than the initial radical concentration at 700 K, i.e., the formation of C_4H_4 and C_6H_6 is catalytic. Under these conditions, the kinetic model agrees well with the experiment within the estimated uncertainty.

The modeled product concentrations in Figure 4b,d show the predicted branching ratios at 500 and 700 K, as well as the individual contributions of the main isomers of C_4H_5 (n-C_4H_5 and c-C_4H_5) and C_6H_6 (benzene and fulvene). At 500 K, n-C_4H_5 is the dominant C_4H_5 isomer, comprising about two-thirds of the total C_4H_5 concentration, and is formed at a slightly faster rate than C_4H_4, indicating that about 55% of the $C_2H_3 + C_2H_2$ reaction proceeds via R1 and 45% via R2. In contrast, at 700 K, the rate of C_4H_4 formation becomes much faster than C_4H_5 formation, such that about 25% of the reaction proceeds via R1 and 75% via R2 (based on the observed ratio at 0.25 ms). The formation of c-C_4H_5 is also faster at 700 K, and after 1 ms, c-C_4H_5 becomes the dominant C_4H_5 isomer due to the accelerated consumption of n-C_4H_5 by C_2H_2. The branching ratio of benzene and fulvene is relatively insensitive to temperature, with approximately 60% proceeding to benzene and 40% to fulvene. Note that the difference in product rise time between the modeled concentrations and the modeled product signals (Figure 4a,c) is due to the effect of molecular beam sampling.

As discussed above, the TOF-MS signals in these experiments may contain contributions from several isomers. The signal at C_6H_6 is expected to contain contributions from both benzene and fulvene. While the PICS for benzene has been determined, no reliable PICS value is available for fulvene at 10.48 eV; based on previous measurements, we assume here that the PICS of
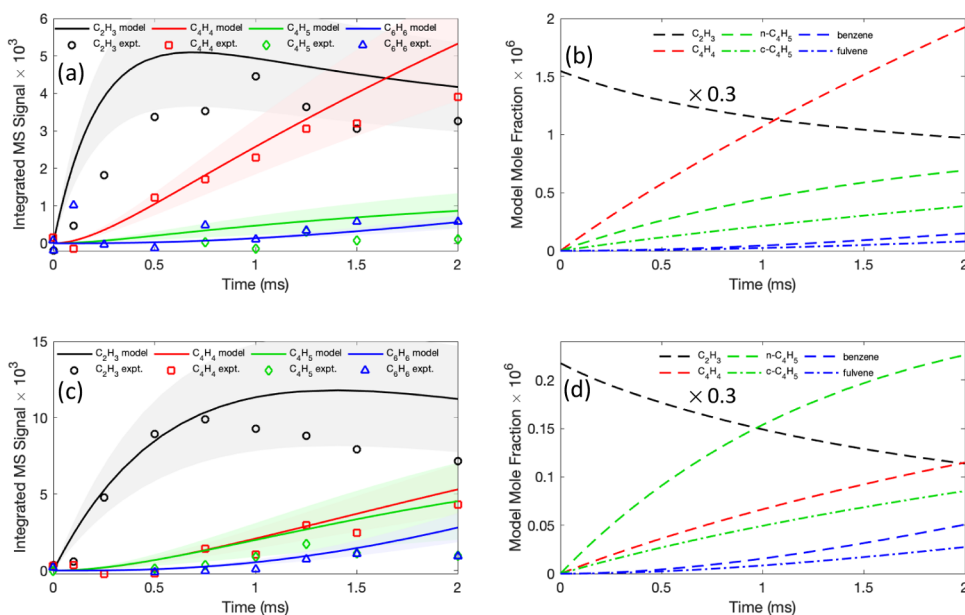
Figure 5. Pressure dependence of measured and modeled TOF-MS signal intensities and modeled species concentrations predicted by model 1 at various delay times after photolysis (time 0). Black circles correspond to the experimental signal for m/z 27 (C_2H_3); red squares, m/z 52 (C_4H_4); green diamonds, m/z 53 (C_4H_5); and blue triangles, m/z 78 (C_6H_6). Solid black, red, green, and blue lines correspond to the modeled signal intensities for C_2H_3, C_4H_4, C_4H_5, and C_6H_6, respectively. Dashed black lines indicate the modeled concentration of C_2H_3 (scaled by a factor of 0.3); dashed red lines, C_4H_4; dashed green lines, n-C_4H_5; dot-dash green lines, c-C_4H_5; dashed blue lines, benzene; and dot-dash blue lines, fulvene. Concentration of C_2H_2: 3 × 10^{16} cm^{-3}. (a, b) 500 K, 5 Torr, $[C_2H_3]_0$ in model = 5 × 10^{11} cm^{-3}; (c, d) 500 K, 50 Torr, $[C_2H_3]_0$ = 7 × 10^{11} cm^{-3}.

fulvene is equivalent to that of benzene (PICS values used in this work are tabulated in the Supporting Information).[58,59] The signal at C_4H_5 could come from either n-C_4H_5 or c-C_4H_5, both of which are predicted to form in significant yields under our experimental conditions. Based on a previous estimate available for the PICS of i-C_4H_5,[60] we estimate a value of 11 Mb for the PICS of n-C_4H_5; however, no reported PICS is available for c-C_4H_5. Given the allylic electronic structure of c-C_4H_5, we assume in this work that the PICS of c-C_4H_5 is equivalent to that of C_3H_5, which has previously been measured to be 6.1 Mb.[61]

The pressure dependence of the observed and predicted C_2H_3 + C_2H_2 product distributions was investigated with TOF-MS measurements at 5 and 50 Torr. Figure 5 shows the measured signal intensities of reactants and products, as well as the species concentrations and signal intensities predicted using model 1 (see the next section for a comparison with model 2 at longer reaction times), up to a reaction time of 2 ms. When the reactor pressure is increased from 5 to 50 Torr, the yield of C_4H_4 relative to C_2H_3 decreases and the formation of C_4H_5 relative to C_4H_4 increases, as collisional stabilization of n-C_4H_5 (R1) becomes more favorable over the well-skipping pathway to C_4H_4 (R2). This is demonstrated by the model concentrations in Figure 5b,d and also observed experimentally, as seen in the change in relative signal intensities in Figure 5a,c.

**3.3. Effect of Side Reactions on Secondary Chemistry.** While the agreement between experiment and Model 1 is satisfactory at short reaction times up to 2 ms, experiments conducted at longer reaction times (up to 10−20 ms) reveal significant discrepancies, particularly the overestimation by the model of the signal at m/z 78, corresponding to C_6H_6 products. These discrepancies suggest that to accurately model secondary chemistry in our system, an extended mechanism containing additional side reactions needs to be constructed to compare with the experiment; this mechanism is called model 2. Potential side reactions include reaction with the I atom (e.g., production

of C_4H_5I from C_4H_5 + I, evidenced by the time-dependent signal at m/z 180), reaction with other radicals (e.g., C_6H_8 formed by recombination of C_2H_3 with n-C_4H_5 or c-C_4H_5, producing the signal at m/z 80), and radical loss due to first-order processes (e.g., wall reaction, unimolecular decomposition). The following paragraphs discuss each of these processes and the reactions added to the base mechanism to create model 2. A detailed description of the additional reactions and their literature sources is given in the Supporting Information.

Recombination reactions of the C_2H_3 and C_4H_5 radicals with the I atom and with secondary product radicals may also influence the observed secondary chemistry, as suggested by the appearance of signals at m/z 180 (corresponding to C_4H_5I) and m/z 80 (corresponding to C_6H_8) at longer reaction times; these reactions were therefore added to model 2. A previously reported temperature-dependent rate constant is available for the recombination of C_2H_3 and the I atom to produce C_2H_3I, on the order of 10^{-12} cm^3 s^{-1};[62] however, this value was derived from a complex mechanism used to fit a high-temperature shock tube experiment and may not be applicable to the present experimental conditions. Thus, we chose instead to use the directly measured recombination rate for CH_3 + I from Mulenko,[63] which is slightly faster (about 10^{-11} cm^3 s^{-1}). The same rate constant was assumed for the recombination of n-C_4H_5 with the I atom, given the similar vinylic structure of n-C_4H_5 to C_2H_3. We note that the model is insensitive to the rates of these reactions within at least a factor of 3, indicating that these reactions are likely not important under our experimental conditions. The recombination of c-C_4H_5 with I, on the other hand, may be significant; since c-C_4H_5 is expected to react slowly toward C_2H_2, it persists longer in the reactor and can react with I over long time scales, potentially influencing the formation of C_4H_5I. While no rate has been reported previously for this reaction, the allylic structure of c-C_4H_5 suggests that it may react similarly to the allyl radical, C_3H_5. The reaction of c-C_4H_5 with I
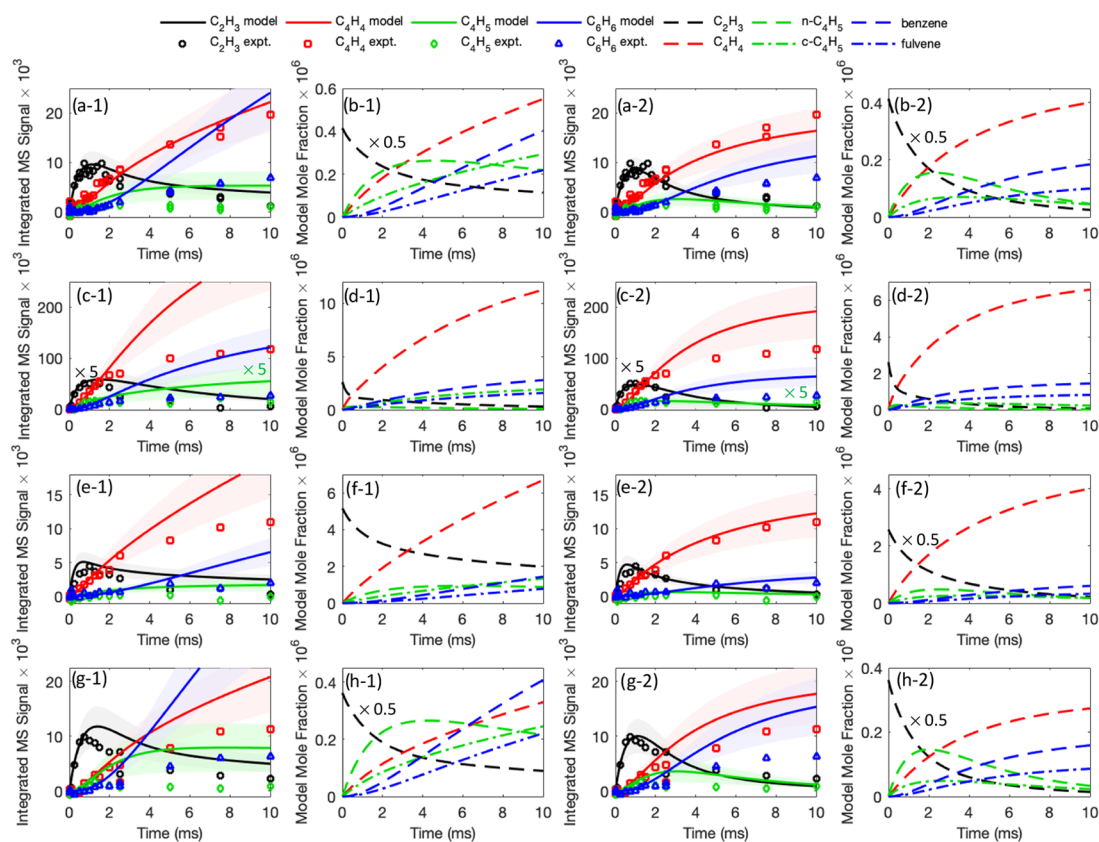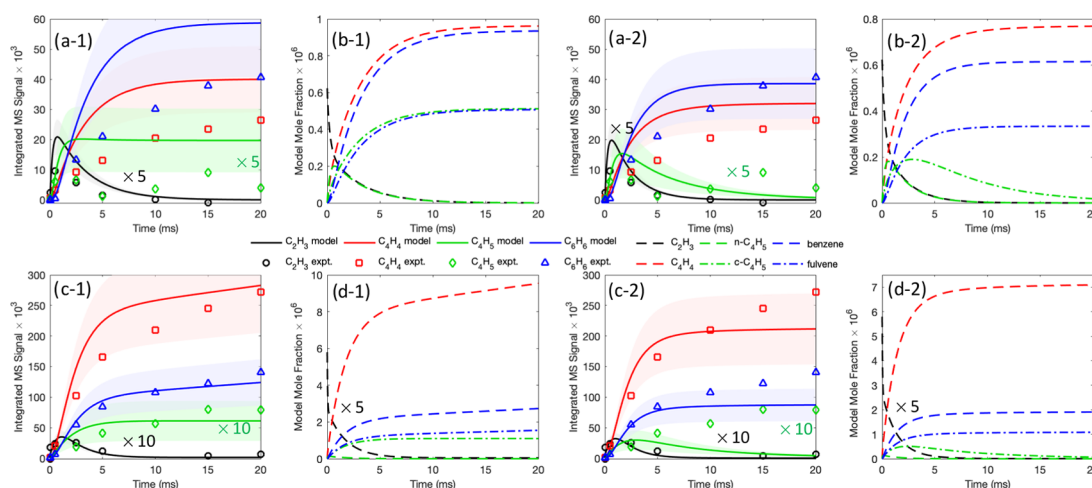
Figure 6. Measured and modeled TOF-MS signal intensities and modeled species concentrations predicted by model 1 (a-1 through h-1) and model 2 (a-2 through h-2) at various delay times up to 10 ms after photolysis (time 0). Black circles correspond to the experimental signal for m/z 27 (C_2H_3, scaled by a factor of 5 for 700 K); red squares, m/z 52 (C_4H_4); green diamonds, m/z 53 (C_4H_5, scaled by a factor of 5 for 700 K); and blue triangles, m/z 78 (C_6H_6). Solid black, red, green, and blue lines correspond to the modeled signal intensities for C_2H_3 (scaled by a factor of 5 for 700 K), C_4H_4, C_4H_5 (scaled by a factor of 5 for 700 K), and C_6H_6, respectively. Dashed black lines indicate the modeled concentration of C_2H_3 (scaled by a factor of 0.5 for 500 K 25 Torr, 500 K 50 Torr, and 500 K 5 Torr model 2); dashed red lines, C_4H_4; dashed green lines, n-C_4H_5; dot-dash green lines, c-C_4H_5; dashed blue lines, benzene; and dot-dash blue lines, fulvene. Concentration of C_2H_2: 3×10^{16} cm^{-3}. (a-1) through (b-2): 500 K, 25 Torr, $[C_2H_3]_0$ in model = 4×10^{11} cm^{-3}; (c-1) through (d-2): 700 K, 25 Torr, 9×10^{11} cm^{-3}; (e-1) through (f-2): 500 K, 5 Torr, $[C_2H_3]_0$ in model = 5×10^{11} cm^{-3}; (g-1) through (h-2): 500 K, 50 Torr, $[C_2H_3]_0 = 7 \times 10^{11}$ cm^{-3}.

was thus included in the model assuming a rate equal to the recombination of C_3H_5 + Br reported by Bedjanian et al.[64] (although a rate for the C_3H_5 + I reaction has been reported by Jenkin et al., on the order of 10^{-11} cm^3 s^{-1}, we suspect that this value may be erroneous since I atom chemistry has been shown to be insignificant in measurements of the C_3H_5 self-reaction[65]).

The reactions of C_2H_3 with the secondary product radicals n-C_4H_5 and c-C_4H_5, producing C_6H_8 at m/z 80, were also added to the model. No rates have been directly determined for these reactions; thus, the reaction of C_2H_3 with n-C_4H_5 was assumed to have the same rate as that of the C_2H_3 self-reaction, while the reaction of C_2H_3 with c-C_4H_5 was assumed to have a rate equal to that reported previously by Tsang[66] for C_2H_3 + C_3H_5 (assuming 100% branching to the recombination product C_6H_8 for both reactions). Reactions of C_4H_5 with other C_4H_5 radicals may also be expected to take place. Although no time-dependent signal was observed at m/z 106, corresponding to the potential recombination product C_8H_{10}, these reactions were nevertheless added to the model to account for any small changes to C_4H_5 concentration that may result from these processes. The self-reaction of n-C_4H_5 was assumed equivalent to the C_2H_3 self-reaction; the self-reaction of c-C_4H_5 was assumed equivalent to the C_3H_5 self-reaction;[67] and the reaction of n-C_4H_5 with c-C_4H_5 was assumed equivalent to the reaction of C_2H_3 with C_3H_5[66] (assuming 100% branching to C_8H_{10} for all

reactions). Recombination reactions with the H atom were also considered: the rate for the reaction of C_2H_3 with H was taken from Fahr et al.,[68] and the same rate was assumed for n-C_4H_5 + H, while the rate for the c-C_4H_5 reaction with H was assumed to be equal to the rate for C_3H_5 + H reported by Tsang.[66] Finally, the pressure-dependent recombinations of I + I and H + I were added to the model, using the rate coefficients provided by Baulch[69] and Lifshitz et al.,[70] respectively.

While radical recombination has a clear impact on the chemistry at long time scales, other reactions involving I atoms may also play a role in scavenging C_2H_3 and C_4H_5 radicals. In addition to recombination, the reaction of C_2H_3 + I might also proceed via a disproportionation channel to produce C_2H_2 + HI. An estimated rate constant for the disproportionation reaction of C_2H_3 + Cl is available from Wakamatsu and Hidaka,[71] and the same value was used here to account for disproportionation reactions of C_2H_3, n-C_4H_5, and c-C_4H_5 with the I atom. Similarly, the reaction of C_2H_3 with HI can proceed via hydrogen abstraction to form C_2H_4 and I as determined by Seetula,[72] and the rate coefficient for this reaction was added to model 2 for both C_2H_3 and n-C_4H_5 radicals, while the rate of C_3H_5 + HI reported by Rossi and Golden[73] was used for the analogous reaction involving c-C_4H_5. Reactions may also occur between radicals and the vinyl iodide precursor, C_2H_3I. No estimates are available in the literature for these reaction rates,

Figure 7. Measured and modeled TOF-MS signal intensities and modeled species concentrations predicted by model 1 (a-1 through d-1) and model 2 (a-2 through d-2) at various delay times up to 20 ms after photolysis (time 0). Black circles correspond to the experimental signal for m/z 27 (C_2H_3, scaled by a factor of 5 for 500 K and 10 for 700 K); red squares, m/z 52 (C_4H_4); green diamonds, m/z 53 (C_4H_5, scaled by a factor of 5 for 500 K and 10 for 700 K); and blue triangles, m/z 78 (C_6H_6). Solid black, red, green, and blue lines correspond to the modeled signal intensities for C_2H_3 (scaled by a factor of 5 for 500 K and 10 for 700 K), C_4H_4, C_4H_5 (scaled by a factor of 5 for 500 K and 10 for 700 K), and C_6H_6, respectively. Dashed black lines indicate the modeled concentration of C_2H_3 (scaled by a factor of 5 for 500 K); dashed red lines, C_4H_4; dashed green lines, n-C_4H_5; dot-dash green lines, c-C_4H_5; dashed blue lines, benzene; and dot-dash blue lines, fulvene. (a-1) through (b-2): 500 K, 25 Torr, $[C_2H_3]_0$ in model = 3×10^{11} cm^{-3}, 2×10^{17} cm^{-3} C_2H_2; (c-1) through (d-2): 700 K, 25 Torr, $[C_2H_3]_0$ in model = 4×10^{11} cm^{-3}, 1.5×10^{17} cm^{-3} C_2H_2.

but a rate for the reaction of the Cl atom with C_2H_4 has been reported[74] and was used in this work for the reaction of I with C_2H_3I. For the reactions of C_2H_3 and C_4H_5 radicals with the vinyl iodide precursor, the rate for each was taken as equal to the reported rate of $C_2H_4 + CH_3$.[75]

First-order loss processes are difficult to quantify in this experiment, but the rate of decomposition of C_2H_3 is well known to be negligible at low pressures and temperatures below 1000 K,[76,77] and other first-order loss processes (wall-catalyzed recombination reactions, diffusion out of the sampling region) were minimized using sufficient C_2H_2 concentrations to ensure a bimolecular loss rate 5–10 times faster than that expected for first-order loss (typically several hundred s^{-1}).[52] Nevertheless, experiments on other reaction systems using the same apparatus indicate that there is likely some impact from wall reactions. Based on previous estimates of radical wall loss in our apparatus (which is primarily expected to involve recombination with the H atom on the walls of the reactor),[52] a first-order loss rate of 100 s^{-1} was assumed for C_2H_3, n-C_4H_5, and c-C_4H_5. This value did not significantly impact major species concentrations in the model but improved the prediction of the kinetic behavior of the C_2H_3 reactant at long times, as well as the appearance of C_4H_6 as a product of wall-catalyzed $C_4H_5 + H$ recombination (C_2H_4, the expected C_2H_3 wall reaction product, could not be observed in our experiment due to its high photoionization energy).

The above reactions and their rates, in addition to the model 1 base mechanism, were used to construct model 2. We note that the reaction rates assumed here for these various side processes are rough estimates intended only for the purpose of evaluating the impact of side chemistry under our experimental conditions and should not be used in other chemical mechanisms. A comparison of model 2 with the experimental signals corresponding to key side products (C_6H_7, C_4H_6, C_6H_8, HI, and C_4H_5I) can be found in the Supporting Information.

Figure 6 shows the measured and predicted TOF-MS signals for both model 1 and model 2 at various temperatures and pressures as in Figures 4 and 5 but extended to reaction times up

to 10 ms. Under these conditions, the secondary chemistry leading to C_6H_6 formation can be clearly observed. While model 1 overpredicts the formation of C_4H_4 and C_6H_6, as well as C_4H_5, model 2 can obtain much closer agreement with the experiment although some discrepancies still remain, likely primarily due to the uncertainties in the rates of various side reactions.

3.4. TOF-MS Experiments at High C_2H_2 Concentrations. As seen above, the increasing effect of side chemistry at reaction times greater than ~1−2 ms with $[C_2H_2] = 3 \times 10^{16}$ cm^{-3} makes it difficult to adequately assess the validity of the potential energy surface for n-$C_4H_5 + C_2H_2$ or the relative branching to C_4H_4 and C_6H_6 without accounting for the side processes in some way, since the formation of C_4H_4 by β-scission of n-C_4H_5 may become more important at longer times, and at lower temperatures, reaction R4 forms significant yields of C_6H_6 only at reaction times greater than 5 ms. To circumvent this issue, we performed experiments using high concentrations of C_2H_2 ($[C_2H_2] = 1.5−2 \times 10^{17}$ cm^{-3}), such that reactions R1−R4 dominate over the side chemistry. These experiments allowed us to investigate the yields of stable products after many reaction steps, since the consumption of radicals via reactions with C_2H_2 became much faster than any potential side reactions.

The results are shown in Figure 7 for 500 and 700 K. At high $[C_2H_2]$, the rate of R5 as well as those of R1−R4 are accelerated, such that the radical chain reaction R1 + R4 + R5 has a long chain length and yields of the stable products C_4H_4 and C_6H_6 are much larger than the initial concentration of C_2H_3. The predictions of the stable product species (C_4H_4 and C_6H_6) by both model 1 and model 2 in Figure 7 agree reasonably well with the measurements within the experimental uncertainty, indicating that the present work satisfactorily validates the previous theoretical calculations of potential energy surfaces for R1−R5.[24,46,78]

At 500 K, the experimental signal at m/z 53 is negligible, yet the model 1 prediction predicts a significant concentration of C_4H_5. The model predicts the C_4H_5 signal to come primarily from c-C_4H_5 at longer reaction times, which is expected to be

unreactive toward C_2H_2 and thus still susceptible to side chemistry despite the increased C_2H_2 concentration. The prediction of model 2, which includes consumption of c-C_4H_5 by side reactions at long time scales, achieves better agreement with the experimental C_4H_5 signal. In contrast, the measured m/z 53 signal gradually increases over long reaction times at 700 K in Figure 7, in excess of the contribution from the ^{13}C analogue of C_4H_4, which has already been subtracted from the experimental signal. While the prediction of model 1 for C_4H_5 agrees well with the experimental signal, model 2 underestimates the signal at long reaction times. This discrepancy might be partially attributed to uncertainties in the side reaction rates in model 2, several of which were determined close to room temperature and do not include temperature dependence. As can be seen in the Supporting Information, the model 2 prediction of observed side products (C_6H_7, C_4H_6, C_6H_8, HI, and C_4H_5I), as well as the kinetic behavior of the I atom, achieves qualitative agreement with the experiment; however, the secondary products containing the I atom, HI and C_4H_5I, are generally underpredicted.

Other impurities in the system may also have an effect at long reaction times; potential acetone impurities in C_2H_2, while mostly removed by the activated charcoal filter (see Section 2), might be photolyzed to produce significant yields of the CH_3 radical when the C_2H_2 concentration is high. Indeed, although no signal is observed at m/z 15, minor time-dependent signals at m/z 41, 42, 66, 67, 68, and 168 appear in the mass spectra for the high [C_2H_2] experiments (see the Supporting Information), possibly corresponding to CH_3 radical reactions with C_2H_2, C_2H_3, C_4H_4, C_4H_5, and C_4H_5I. Based on our assessment of the model sensitivity to these reactions, we estimate that photolytically generated CH_3, in the worst case, could cause up to 5−10% variation in the concentrations of the major reactants and products.

Another potential contribution to the C_4H_5 signal, particularly at higher c-C_4H_5 radical concentrations as in the experiments in Figure 7, may arise from radical reactions with the I atom, which lead to fragmentation in the mass spectrometer, a phenomenon that has been observed in previous experiments using this apparatus.[52] For example, ionized C_4H_5I may fragment to produce $C_4H_5^+$ in the ionization region, producing an artifact signal at m/z 53 at longer reaction times. To assess the possible impact of C_4H_5I fragmentation on the m/z 53 signal, we included a fragmentation factor f in model 2 by adding a fraction of the modeled C_4H_5I signal to the modeled C_4H_5 signal at each reaction condition. Figure 8 illustrates the effect of varying f between 0 (no C_4H_5I fragmentation) and 1 (100% C_4H_5I fragmentation to $C_4H_5^+$) for the high [C_2H_2] experiments. Increased fragmentation leads to a rise in the m/z 53 signal at longer time scales and assuming $f = 0.5$ achieves a closer agreement with the measured signal at both 500 and 700 K. The effect of fragmentation was also tested for the lower [C_2H_2] experiments discussed in Sections 3.1 and 3.2; the results are given in the Supporting Information. The magnitude of the signal due to fragmented C_4H_5I in the model is dependent on the predicted concentration of C_4H_5I, which is generally lower than the C_4H_5I concentration observed in the experiment (see the modeled and experimental signals of side products in the Supporting Information). Increasing the rate of C_4H_5I formation could result in an increase in the predicted m/z 53 signal due to the effect of fragmentation, thus further improving the agreement between the model and the experiment in Figure 8b-2.
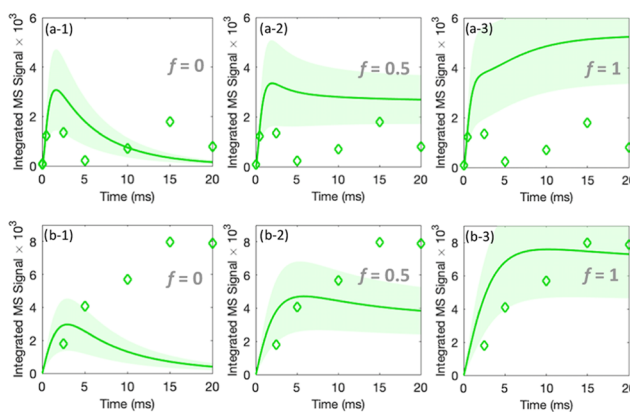
Figure 8. Time-resolved background-corrected measured (symbols) and modeled (lines) signal intensities predicted with model 2 for C_4H_5 (m/z 53). The fragmentation factor f indicates the fraction of C_4H_5I fragmented to $C_4H_5^+$ in the model. (a-1) through (a-3): 500 K, 25 Torr, [C_2H_3]$_0$ in model = 3×10^{11} cm^{-3}, 2×10^{17} cm^{-3} C_2H_2; (b-1) through (b-3): 700 K, 25 Torr, [C_2H_3]$_0$ in model = 4×10^{11} cm^{-3}, 1.5×10^{17} cm^{-3} C_2H_2.

In summary, the discrepancies between the modeled and measured C_4H_5 signals at longer reaction times in our experiments most likely arise from a combination of the uncertainty in PICS, uncertainties in the rate estimates for side reactions in model 2, and potential C_4H_5I fragmentation in the mass spectrometer. However, these discrepancies primarily affect the predicted concentration of c-C_4H_5, which does not impact the main $C_2H_3 + C_2H_2$ and n-$C_4H_5 + C_2H_2$ reaction systems, which are the focus of this work.

The pressure- and temperature-dependent rate coefficients calculated in this work represent a marked improvement over typical values used in combustion mechanisms. Importantly, the rate coefficient validated here for C_4H_5 formation from $C_2H_3 + C_2H_2$ at temperatures above 500 K deviates by an order of magnitude or higher from earlier predictions,[22,45] which are used in well-known models including the Narayanaswamy[79,80] and JetSurF 2.0[81] mechanisms. As a demonstration of this point, we have simulated model 1 under our experimental conditions including reaction rate coefficients for $C_2H_3 + C_2H_2$ and n-C_4H_5 + C_2H_2 used in Narayanaswamy and JetSurF 2.0; the results are shown in the Supporting Information. We recommend our validated rates be used in future mechanism development efforts.

4. CONCLUSIONS

The temperature- and pressure-dependent kinetics and product yields from the $C_2H_3 + C_2H_2$ reaction were studied using time-resolved photoionization time-of-flight mass spectrometry (PI-TOF-MS) at 500 and 700 K and 5−50 Torr. Significant temperature- and pressure-dependent yields of C_4H_5, C_4H_4, and C_6H_6 were observed. The catalytic cycle leading to formation of C_4H_4 and C_6H_6 can be clearly observed under our experimental conditions (i.e., much higher yields of products than the number of initial radicals), and the radical chain reactions responsible for these high product yields are elucidated by comparison with a pressure-dependent kinetic mechanism constructed from experimental and calculated reaction rates. Branching to the H-loss channel producing C_4H_4 increased with increasing temperature and decreasing pressure, while the yield of n-C_4H_5 from collisional stabilization increased with increasing pressure, indicating that C_4H_4 is formed primarily via the

chemically activated pathway. The yield of C_6H_6 also increased at higher temperatures due to the increasing reaction rate of n-C_4H_5 + C_2H_2. To model the secondary chemistry leading to C_6H_6 formation at long time scales, several side reactions were added to the model to estimate the effect of wall reactions, reactions with the I atom, and radical−radical reactions. Additional experiments performed at high C_2H_2 concentrations produced large yields of C_4H_4 and C_6H_6, which were adequately predicted by the model without needing to account for side chemistry.

This work provides direct experimental evidence of the n-C_4H_5 radical intermediate formed from C_2H_3 addition to C_2H_2 and its subsequent reaction to form benzene and validates the most recent theoretical predictions of these reactions for use in complex combustion mechanisms. The rates validated in this work, which are derived from recent *ab initio* calculations,[46] are consistent with previous measurements at low temperatures[21] as well as with the higher-temperature (500 and 700 K) experiments presented here. Hence, the experiments in this work together with previous measurements cover the region of the potential energy surface that is the most sensitive to temperature and pressure, which gives us confidence that the validated mechanism can be used to predict accurate rates when extended to combustion-relevant conditions.

ASSOCIATED CONTENT

Supporting Information

The Supporting Information is available free of charge at https://pubs.acs.org/doi/10.1021/acs.jpca.0c00558.

> Schematic of experimental apparatus; photoionization cross sections used in the kinetic model; detailed kinetic mechanism; time-resolved 2D-MS spectra of m/z 27; TOF-MS measured and modeled signals of side products; model simulations including reaction rates from JetSurF 2.0 and Narayanaswamy mechanisms; model sensitivity analysis (PDF)

> Annotated Chemkin input file for the kinetic model (TXT)

AUTHOR INFORMATION

Corresponding Author

William H. Green − *Department of Chemical Engineering, Massachusetts Institute of Technology, Cambridge, Massachusetts 01239, United States;* orcid.org/0000-0003-2603-9694; Phone: +617-253-4580; Email: whgreen@mit.edu

Authors

Mica C. Smith − *Department of Chemical Engineering, Massachusetts Institute of Technology, Cambridge, Massachusetts 01239, United States;* orcid.org/0000-0003-4534-7246

Guozhu Liu − *Department of Chemical Engineering, Massachusetts Institute of Technology, Cambridge, Massachusetts 01239, United States; Key Laboratory for Green Chemical Technology of the Ministry of Education, School of Chemical Engineering and Technology, Collaborative Innovation Center of Chemical Science and Engineering (Tianjin), Tianjin University, Tianjin 300072, China;* orcid.org/0000-0003-2193-5289

Zachary J. Buras − *Department of Chemical Engineering, Massachusetts Institute of Technology, Cambridge, Massachusetts 01239, United States;* orcid.org/0000-0001-8831-6218

Te-Chun Chu − *Department of Chemical Engineering, Massachusetts Institute of Technology, Cambridge, Massachusetts 01239, United States;* orcid.org/0000-0002-8475-7697

Jeehyun Yang − *Department of Earth, Atmospheric, and Planetary Sciences, Massachusetts Institute of Technology, Cambridge, Massachusetts 01239, United States*

Complete contact information is available at:
https://pubs.acs.org/10.1021/acs.jpca.0c00558

Notes

The authors declare no competing financial interest.

REFERENCES

(1) Miller, J. A. Theory and Modeling in Combustion Chemistry. *Proc. Combust. Inst.* **1996**, *26*, 461−480.

(2) Richter, H.; Howard, J. B. Formation of Polycyclic Aromatic Hydrocarbons and Their Growth to Soot—a Review of Chemical Reaction Pathways. *Prog. Energy Combust. Sci.* **2000**, *26*, 565−608.

(3) Wang, H. Formation of Nascent Soot and Other Condensed-Phase Materials in Flames. *Proc. Combust. Inst.* **2011**, *33*, 41−67.

(4) Bittner, J. D.; Howard, J. B. Composition Profiles and Reaction Mechanisms in a Near-Sooting Premixed Benzene/Oxygen/Argon Flame. *Proc. Combust. Inst.* **1981**, *18*, 1105−1116.

(5) Frenklach, M.; Clary, D. W.; Gardiner, W. C.; Stein, S. E. Detailed Kinetic Modeling of Soot Formation in Shock-Tube Pyrolysis of Acetylene. *Proc. Combust. Inst.* **1985**, *20*, 887−901.

(6) Frenklach, M.; Wang, H. Detailed Modeling of Soot Particle Nucleation and Growth. *Proc. Combust. Inst.* **1991**, *23*, 1559−1566.

(7) Frenklach, M. Reaction Mechanism of Soot Formation in Flames. *Phys. Chem. Chem. Phys.* **2002**, *4*, 2028−2037.

(8) Wang, Y.; Chung, S. H. Soot Formation in Laminar Counterflow Flames. *Prog. Energy Combust. Sci.* **2019**, *74*, 152−238.

(9) Hansen, N.; Klippenstein, S. J.; Taatjes, C. A.; Miller, J. A.; Wang, J.; Cool, T. A.; Yang, B.; Yang, R.; Wei, L.; Huang, C.; et al. Identification and Chemistry of C_4H_3 and C_4H_5 Isomers in Fuel-Rich Flames. *J. Phys. Chem. A* **2006**, *110*, 3670−3678.

(10) Li, Y.; Zhang, L.; Tian, Z.; Yuan, T.; Wang, J.; Yang, B.; Qi, F. Experimental Study of a Fuel-Rich Premixed Toluene Flame at Low Pressure. *Energy Fuels* **2009**, *23*, 1473−1485.

(11) Li, Y.; Zhang, L.; Yuan, T.; Zhang, K.; Yang, J.; Yang, B.; Qi, F.; Law, C. K. Investigation on Fuel-Rich Premixed Flames of Monocyclic Aromatic Hydrocarbons: Part I. Intermediate Identification and Mass Spectrometric Analysis. *Combust. Flame* **2010**, *157*, 143−154.

(12) Li, W.; Law, M. E.; Westmoreland, P. R.; Kasper, T.; Hansen, N.; Kohse-Höinghaus, K. Multiple Benzene-Formation Paths in a Fuel-Rich Cyclohexane Flame. *Combust. Flame* **2011**, *158*, 2077−2089.

(13) Johansson, K. O.; Head-Gordon, M. P.; Schrader, P. E.; Wilson, K. R.; Michelsen, H. A. Resonance-Stabilized Hydrocarbon-Radical Chain Reactions May Explain Soot Inception and Growth. *Science* **2018**, *361*, 997−1000.

(14) Georgievskii, Y.; Miller, J. A.; Klippenstein, S. J. Association Rate Constants for Reactions between Resonance-Stabilized Radicals: C_3H_3 + C_3H_3, C_3H_3 + C_3H_5, and C_3H_5 + C_3H_5. *Phys. Chem. Chem. Phys.* **2007**, *9*, 4259−4268.

(15) Miller, J. A.; Klippenstein, S. J.; Georgievskii, Y.; Harding, L. B.; Allen, W. D.; Simmonett, A. C. Reactions between Resonance-Stabilized Radicals: Propargyl + Allyl. *J. Phys. Chem. A* **2010**, *114*, 4881−4890.

(16) Miller, J. A.; Klippenstein, S. J. The Recombination of Propargyl Radicals: Solving the Master Equation. *J. Phys. Chem. A* **2001**, *105*, 7254−7266.

(17) Miller, J. A.; Klippenstein, S. J. The Recombination of Propargyl Radicals and Other Reactions on a C_6H_6 Potential. *J. Phys. Chem. A* **2003**, *107*, 7783−7799.

(18) Shafir, E. V.; Slagle, I. R.; Knyazev, V. D. Kinetics and Products of the Self-Reaction of Propargyl Radicals. *J. Phys. Chem. A* **2003**, *107*, 8893−8903.

(19) Sharma, S.; Green, W. H. Computed Rate Coefficients and Product Yields for c-C_5H_5 + CH_3 → Products. *J. Phys. Chem. A* **2009**, *113*, 8871−8882.

(20) Krasnoukhov, V. S.; Porfiriev, D. P.; Zavershinskiy, I. P.; Azyazov, V. N.; Mebel, A. M. Kinetics of the CH_3 + C_5H_5 Reaction: A Theoretical Study. *J. Phys. Chem. A* **2017**, *121*, 9191−9200.

(21) Callear, A. B.; Smith, G. B. Recurring Chains Following Addition of Atomic Hydrogen to Acetylene. *J. Phys. Chem. A* **1986**, *90*, 3229−3237.

(22) Wang, H.; Frenklach, M. Calculations of Rate Coefficients for the Chemically Activated Reactions of Acetylene with Vinylic and Aromatic Radicals. *J. Phys. Chem. B* **1994**, *98*, 11465−11489.

(23) Westmoreland, P. R.; Dean, A. M.; Howard, J. B.; Longwell, J. P. Forming Benzene in Flames by Chemically Activated Isomerization. *J. Phys. Chem. C* **1989**, *93*, 8171−8180.

(24) Senosiain, J. P.; Miller, J. A. The Reaction of n- and i-C_4H_5 Radicals with Acetylene. *J. Phys. Chem. A* **2007**, *111*, 3740−3747.

(25) Huang, C.; Yang, B.; Zhang, F.; Tian, G. Quantification of the Resonance Stabilized C_4H_5 Isomers and Their Reaction with Acetylene. *Combust. Flame* **2018**, *198*, 334−341.

(26) Pope, C. J.; Miller, J. A. Exploring Old and New Benzene Formation Pathways in Low-Pressure Premixed Flames of Aliphatic Fuels. *Proc. Combust. Inst.* **2000**, *28*, 1519−1527.

(27) Nakamura, H.; Tanimoto, R.; Tezuka, T.; Hasegawa, S.; Maruta, K. Soot Formation Characteristics and PAH Formation Process in a Micro Flow Reactor with a Controlled Temperature Profile. *Combust. Flame* **2014**, *161*, 582−591.

(28) Wang, B.-Y.; Liu, Y.-X.; Weng, J.-J.; Glarborg, P.; Tian, Z.-Y. New Insights in the Low-Temperature Oxidation of Acetylene. *Proc. Combust. Inst.* **2017**, *36*, 355−363.

(29) Kathrotia, T.; Oßwald, P.; Köhler, M.; Slavinskaya, N.; Riedel, U. Experimental and Mechanistic Investigation of Benzene Formation during Atmospheric Pressure Flow Reactor Oxidation of N-Hexane, n-Nonane, and n-Dodecane below 1200 K. *Combust. Flame* **2018**, *194*, 426−438.

(30) Wang, E.; Ding, J.; Han, K. Reaction between i-C_4H_3 Radical and Acetylene (C_2H_2): Is Phenyl (C_6H_5) the Primary Product? *Energy Fuels* **2018**, *32*, 5581−5587.

(31) Hansen, N.; Miller, J. A.; Kasper, T.; Kohse-Höinghaus, K.; Westmoreland, P. R.; Wang, J.; Cool, T. A. Benzene Formation in Premixed Fuel-Rich 1,3-Butadiene Flames. *Proc. Combust. Inst.* **2009**, *32*, 623−630.

(32) Moshammer, K.; Seidel, L.; Wang, Y.; Selim, H.; Sarathy, S. M.; Mauss, F.; Hansen, N. Aromatic Ring Formation in Opposed-Flow Diffusive 1,3-Butadiene Flames. *Proc. Combust. Inst.* **2017**, *36*, 947−955.

(33) Benson, S. W. The Mechanism of the Reversible Reaction: $2C_2H_2 \rightleftharpoons$ Vinyl Acetylene and the Pyrolysis of Butadiene. *Int. J. Chem. Kinet.* **1989**, *21*, 233−243.

(34) Benson, S. W. Radical Processes in the Pyrolysis of Acetylene. *Int. J. Chem. Kinet.* **1992**, *24*, 217−237.

(35) Zádor, J.; Fellows, M. D.; Miller, J. A. Initiation Reactions in Acetylene Pyrolysis. *J. Phys. Chem. A* **2017**, *121*, 4203−4217.

(36) Liu, P.; Zhang, Y.; Li, Z.; Bennett, A.; Lin, H.; Sarathy, S. M.; Roberts, W. L. Computational Study of Polycyclic Aromatic Hydrocarbons Growth by Vinylacetylene Addition. *Combust. Flame* **2019**, *202*, 276−291.

(37) Calcote, H. F. Mechanisms of Soot Nucleation in Flames—A Critical Review. *Combust. Flame* **1981**, *42*, 215−242.

(38) Harris, S. J.; Weiner, A. M. Surface Growth of Soot Particles in Premixed Ethylene/Air Flames. *Combust. Sci. Technol.* **1983**, *31*, 155−167.

(39) Knyazev, V. D.; Bencsura, Á.; Stoliarov, S. I.; Slagle, I. R. Kinetics of the C_2H_3 + $H_2 \rightleftharpoons$ H + C_2H_4 and CH_3 + $H_2 \rightleftharpoons$ H + CH_4 Reactions. *J. Phys. Chem. D* **1996**, *100*, 11346−11354.

(40) Fahr, A.; Stein, S. E. Reactions of Vinyl and Phenyl Radicals with Ethyne, Ethene and Benzene. *Proc. Combust. Inst.* **1989**, *22*, 1023−1029.

(41) Ismail, H.; Abel, P. R.; Green, W. H.; Fahr, A.; Jusinski, L. E.; Knepp, A. M.; Zádor, J.; Meloni, G.; Selby, T. M.; Osborn, D. L.; et al. Temperature-Dependent Kinetics of the Vinyl Radical (C_2H_3) Self-Reaction. *J. Phys. Chem. A* **2009**, *113*, 1278−1286.

(42) Kubitza, C. Das Vinylradikal - Massenspektrometrische Untersuchungen Seiner Radikal-Radikal-Reaktionen Und Seiner Additionsreaktionen Mit Ungesättigten Kohlenwasserstoffen in Der Gasphase. Doctoral Dissertation, Technischen Hochschule: Darmstadt, Germany, 1996.

(43) Knyazev Vadim, D.; Stoliarov, S. I.; Slagle, I. R. Kinetics of the Reaction of Vinyl Radicals with Acetylene. *Proc. Combust. Inst.* **1996**, *26*, 513−519.

(44) Weissman, M. A.; Benson, S. W. Rate Parameters for the Reactions of Vinyl and Butadienyl Radicals with Hydrogen and Acetylene. *J. Phys. Chem. E* **1988**, *92*, 4080−4084.

(45) Miller, J. A.; Klippenstein, S. J.; Robertson, S. H. A Theoretical Analysis of the Reaction between Vinyl and Acetylene: Quantum Chemistry and Solution of the Master Equation. *J. Phys. Chem. A* **2000**, *104*, 7525−7536.

(46) Ribeiro, J. M.; Mebel, A. M. Reaction Mechanism and Product Branching Ratios of the CH + C_3H_4 Reactions: A Theoretical Study. *Phys. Chem. Chem. Phys.* **2017**, *19*, 14543−14554.

(47) Melius, C. F.; Colvin, M. E.; Marinov, N. M.; Pit, W. J.; Senkan, S. M. Reaction Mechanisms in Aromatic Hydrocarbon Formation Involving the C_5H_5 Cyclopentadienyl Moiety. *Proc. Combust. Inst.* **1996**, *26*, 685−692.

(48) Sharma, S.; Harper, M. R.; Green, W. H. Modeling of 1,3-Hexadiene, 2,4-Hexadiene and 1,4-Hexadiene-Doped Methane Flames: Flame Modeling, Benzene and Styrene Formation. *Combust. Flame* **2010**, *157*, 1331−1345.

(49) Jasper, A. W.; Hansen, N. Hydrogen-Assisted Isomerizations of Fulvene to Benzene and of Larger Cyclic Aromatic Hydrocarbons. *Proc. Combust. Inst.* **2013**, *34*, 279−287.

(50) Miller, J. A.; Klippenstein, S. J. The H + C_2H_2 (+M) $\rightleftharpoons$ C_2H_3 (+M) and H + C_2H_2 (+M) $\rightleftharpoons$ C_2H_5 (+M) Reactions: Electronic Structure, Variational Transition-State Theory, and Solutions to a Two-Dimensional Master Equation. *Phys. Chem. Chem. Phys.* **2004**, *6*, 1192−1202.

(51) Middaugh, J. E.; Buras, Z. J.; Matrat, M.; Chu, T.-C.; Kim, Y.-S.; Alecu, I. M.; Vasiliou, A. K.; Goldsmith, C. F.; Green, W. H. A Combined Photoionization Time-of-Flight Mass Spectrometry and Laser Absorption Spectrometry Flash Photolysis Apparatus for Simultaneous Determination of Reaction Rates and Product Branching. *Rev. Sci. Instrum.* **2018**, *89*, No. 074102.

(52) Buras, Z. J.; Chu, T.-C.; Jamal, A.; Yee, N. W.; Middaugh, J. E.; Green, W. H. Phenyl Radical + Propene: A Prototypical Reaction Surface for Aromatic-Catalyzed 1,2-Hydrogen-Migration and Subsequent Resonance-Stabilized Radical Formation. *Phys. Chem. Chem. Phys.* **2018**, *20*, 13191−13214.

(53) Allen, J. W.; Goldsmith, C. F.; Green, W. H. Automatic Estimation of Pressure-Dependent Rate Coefficients. *Phys. Chem. Chem. Phys.* **2012**, *14*, 1131−1155.

(54) Joback, K. G.; Reid, R. C. Estimation of Pure-Component Properties from Group-Contributions. *Chem. Eng. Comm.* **1987**, *57*, 233−243.

(55) Gao, C. W.; Allen, J. W.; Green, W. H.; West, R. H. Reaction Mechanism Generator: Automatic Construction of Chemical Kinetic Mechanisms. *Comput. Phys. Commun.* **2016**, *203*, 212−225.

(56) Chu, T.-C.; Buras, Z. J.; Eyob, B.; Smith, M. C.; Liu, M.; Green, W. H. Direct Kinetics and Product Measurement of Phenyl Radical + Ethylene. *J. Phys. Chem. A* **2020**, DOI: 10.1021/acs.jpca.9b11543.

(57) Diau, E. W.; Lin, M. C.; Melius, C. F. A Theoretical Study of the $CH_3 + C_2H_2$ Reaction. *J. Chem. Phys.* **1994**, *101*, 3923−3927.

(58) Cool, T. A.; Wang, J.; Nakajima, K.; Taatjes, C. A.; McIlroy, A. Photoionization Cross Sections for Reaction Intermediates in Hydrocarbon Combustion. *Int. J. Mass Spectrom.* **2005**, *247*, 18−27.

(59) Hansen, N.; Miller, J. A.; Taatjes, C. A.; Wang, J.; Cool, T. A.; Law, M. E.; Westmoreland, P. R. Photoionization Mass Spectrometric Studies and Modeling of Fuel-Rich Allene and Propyne Flames. *Proc. Combust. Inst.* **2007**, *31*, 1157−1164.

(60) Li, Y. Y.; Yang, J. Z.; Cheng, Z. J.. *Photoionization Cross Section Database (Version 2.0)*. http://flame.nsrl.ustc.edu.cn/database/.

(61) Robinson, J. C.; Sveum, N. E.; Neumark, D. M. Determination of Absolute Photoionization Cross Sections for Isomers of C_3H_5: Allyl and 2-Propenyl Radicals. *Chem. Phys. Lett.* **2004**, *383*, 601−605.

(62) Lifshitz, A.; Tamburu, C.; Dubnikova, F. Reactions of 1-Naphthyl Radicals with Ethylene. Single Pulse Shock Tube Experiments, Quantum Chemical, Transition State Theory, and Multiwell Calculations. *J. Phys. Chem. A* **2008**, *112*, 925−933.

(63) Mulenko, S. A. The Application of an Intracavity Laser Spectroscopy Method for Elementary Processes Study in Gas-Phase Reactions. *Rev. Roum. Phys.* **1987**, *32*, 173−178.

(64) Bedjanian, Y.; Poulet, G.; Bras, G. L. Low-Pressure Study of the Reactions of Br Atoms with Alkenes. 1. Reaction with Propene. *J. Phys. Chem. A* **1998**, *102*, 5867−5875.

(65) Jenkin, M. E.; Murrells, T. P.; Shalliker, S. J.; Hayman, G. D. Kinetics and Product Study of the Self-Reactions of Allyl and Allyl Peroxy Radicals at 296 K. *Faraday Trans.* **1993**, *89*, 433.

(66) Tsang, W. Chemical Kinetic Data Base for Combustion Chemistry Part V. Propene. *J. Phys. Chem. Ref. Data* **1991**, *20*, 221−273.

(67) Ismail, H. Addition and Recombination Reactions of Unsaturated Radicals Using a Novel Laser Kinetics Spectrometer. Doctoral Dissertation, Massachusetts Institute of Technology, 2008.

(68) Fahr, A.; Laufer, A.; Klein, R.; Braun, W. Reaction Rate Determinations of Vinyl Radical Reactions with Vinyl, Methyl, and Hydrogen Atoms. *J. Phys. Chem. F* **1991**, *95*, 3218−3224.

(69) Baulch, D. L.; Duxbury, J.; Grant, S. J.; Montague, D. C. Evaluated Kinetic Data for High Temperature Reactions, Volume 4: Homogeneous Gas Phase Reactions of Halogen- and Cyanide-Containing Species. *J. Phys. Chem. Ref. Data* **1981**, 1−721.

(70) Lifshitz, A.; Tamburu, C.; Dubnikova, F. Reactions of 1-Naphthyl Radicals with Acetylene. Single-Pulse Shock Tube Experiments and Quantum Chemical Calculations. Differences and Similarities in the Reaction with Ethylene. *J. Phys. Chem. A* **2009**, *113*, 10446−10451.

(71) Wakamatsu, H.; Hidaka, Y. Shock-Tube and Modeling Study of Chloroethane Pyrolysis and Oxidation. *Int. J. Chem. Kinet.* **2008**, *40*, 320−339.

(72) Seetula, J. A. Kinetics, Thermochemistry and Reactivity of Reactions of Some Polyatomic Free Radicals with HI, HBr, Cl_2 and Br_2. *In Annales Academiae Scientiarum Fennicae, Series A2 Chemica* **1991**, 1−45.

(73) Rossi, M.; Golden, D. M. Absolute Rate Constants for Metathesis Reactions of Allyl and Benzyl Radicals with Hydriodic Acid (Hydriodic Acid-d). Heat of Formation of Allyl and Benzyl Radicals. *J. Am. Chem. Soc.* **1979**, *101*, 1230−1235.

(74) Pilgrim, J. S.; Taatjes, C. A. Infrared Absorption Probing of the Cl + C_2H_4 Reaction: Direct Measurement of Arrhenius Parameters for Hydrogen Abstraction. *J. Phys. Chem. A* **1997**, *101*, 4172−4177.

(75) Baulch, D. L.; Cobos, C. J.; Cox, R. A.; Esser, C.; Frank, P.; Just, T.; Kerr, J. A.; Pilling, M. J.; Troe, J.; Walker, R. W.; et al. Evaluated Kinetic Data for Combustion Modelling. *J. Phys. Chem. Ref. Data* **1992**, *21*, 411−734.

(76) Li, Y.; Brenner, D. W.; Dong, X.; Sun, C. Ab Initio Study of the Role of Entropy in the Kinetics of Acetylene Production in Filament-Assisted Diamond Growth Environments. *J. Phys. Chem. A* **2006**, *110*, 132−140.

(77) Knyazev, V. D.; Slagle, I. R. Experimental and Theoretical Study of the $C_2H_3 \rightleftarrows H + C_2H_2$ Reaction. Tunneling and the Shape of Falloff Curves. *J. Phys. Chem. G* **1996**, *100*, 16899−16911.

(78) Miller, J. A.; Klippenstein, S. J.; Robertson, S. H. A Theoretical Analysis of the Reaction between Vinyl and Acetylene: Quantum Chemistry and Solution of the Master Equation. *J. Phys. Chem. A* **2000**, *104*, 9806.

(79) Laskin, A.; Wang, H.; Wang, C. K. Detailed Kinetic Modeling of 1,3-Butadiene Oxidation at High Temperatures. *Int. J. Chem. Kinet.* **2000**, *32*, 589−614.

(80) Narayanaswamy, K.; Blanquart, G.; Pitsch, H. A Consistent Chemical Mechanism for Oxidation of Substituted Aromatic Species. *Combust. Flame* **2010**, *157*, 1879−1898.

(81) Wang, H.; Dames, E.; Sirjean, B.; Sheen, D. A.; Tango, R.; Violi, A.; Lai, J. Y. W.; Egolfopoulos, F. N.; Davidson, D. F.; Hanson, R. K. et al. *A High-Temperature Chemical Kinetic Model of n-Alkane (up to n-Dodecane),Cyclohexane, and Methyl-, Ethyl-, n-Propyl and n-Butyl-Cyclohexane Oxidation at High Temperatures*, JetSurF version 2.0, September 19, 2010. http://web.stanford.edu/group/haiwanglab/JetSurF/JetSurF2.0/index.html.